The Astrophysical Journal Letters, 993:L18 (10pp), 2025 November 1 https://doi.org/10.3847/2041-8213/ae0d8b

H I Properties of Field Galaxies at $z \approx 0.2$–0.6: Insights into Declining Cosmic Star Formation

David DePalma[1], Neeraj Gupta[2], Hsiao-Wen Chen[3], Robert A. Simcoe[1], Sergei Balashev[4], Erin Boettcher[5,6,7], Sebastiano Cantalupo[8], Mandy C. Chen[9,10], Françoise Combes[11], Claude-André Faucher-Giguère[12], Sean D. Johnson[13], Hans-Rainer Klöckner[14], Jens-Kristian Krogager[15,16], Jennifer I-Hsiu Li[17], Sebastián López[18], Pasquier Noterdaeme[19], Patrick Petitjean[19], Zhijie Qu[20], Gwen C. Rudie[10], Joop Schaye[21], and Fakhri Zahedy[22]
[1] MIT–Kavli Institute for Astrophysics and Space Research, 77 Massachusetts Avenue, Cambridge, MA 02139, USA; ddepalma@mit.edu
[2] Inter-University Centre for Astronomy and Astrophysics, Post Bag 4, Ganeshkhind, Pune 411 007, India
[3] Department of Astronomy and Astrophysics, The University of Chicago, 5640 S. Ellis Avenue, Chicago, IL 60637, USA
[4] Independent Researcher
[5] Department of Astronomy, University of Maryland, College Park, MD 20742, USA
[6] X-ray Astrophysics Laboratory, NASA/GSFC, Greenbelt, MD 20771, USA
[7] Center for Research and Exploration in Space Science and Technology, NASA/GSFC, Greenbelt, MD 20771, USA
[8] Department of Physics, University of Milan Bicocca, Piazza della Scienza 3, I-20126 Milano, Italy
[9] Cahill Center for Astronomy and Astrophysics, California Institute of Technology, Pasadena, CA 91125, USA
[10] The Observatories of the Carnegie Institution for Science, 813 Santa Barbara Street, Pasadena, CA 91101, USA
[11] Observatoire de Paris, Collège de France, PSL University, Sorbonne University, CNRS, LUX, Paris, France
[12] CIERA and Department of Physics and Astronomy, Northwestern University, 1800 Sherman Avenue, Evanston, IL 60201, USA
[13] Department of Astronomy, University of Michigan, 1085 S. University, Ann Arbor, MI 48109, USA
[14] Max-Planck-Institut für Radioastronomie, Auf dem Hügel 69, 53121 Bonn, Germany
[15] Université Lyon, ENS de Lyon, CNRS, Centre de Recherche Astrophysique de Lyon UMR5574, 69230 Saint-Genis-Laval, France
[16] French-Chilean Laboratory for Astronomy, IRL 3386, CNRS and Universidad de Chile, Santiago, Chile
[17] Center for AstroPhysical Surveys, National Center for Supercomputing Applications, University of Illinois Urbana-Champaign, Urbana, IL 61801, USA
[18] Departamento de Astronomía, Universidad de Chile, Casilla 36-D, Santiago 7550000, Chile
[19] Institut d'astrophysique de Paris, CNRS-SU, UMR 7095, 98bis bd Arago, 75014 Paris, France
[20] Department of Astronomy E304, Physics Building, Tsinghua University, Beijing, People's Republic of China
[21] Leiden Observatory, Leiden University, PO Box 9513, 2300 RA Leiden, the Netherlands
[22] Department of Physics, University of North Texas, Denton, TX 76201, USA
Received 2025 August 12; revised 2025 September 16; accepted 2025 September 28; published 2025 October 28

Abstract

We report statistically significant detection of H I 21 cm emission from intermediate-redshift ($z \approx 0.2$–0.6) galaxies. By leveraging multisightline galaxy survey data from the Cosmic Ultraviolet Baryon Survey and deep radio observations from the MeerKAT Absorption Line Survey, we have established a sample of ≈6000 spectroscopically identified galaxies in 11 distinct fields to constrain the neutral gas content at intermediate redshifts. The galaxies sample a broad range in stellar mass, from $\log M_{\rm star}/M_{\odot} \approx 8$ to $\log M_{\rm star}/M_{\odot} \approx 11$, with a median of $\langle \log M_{\rm star}/M_{\odot} \rangle_{\rm med} \approx 10$ and a wide range in redshift from $z \approx 0.24$ to $z \approx 0.63$ with a median of $\langle z \rangle_{\rm med} = 0.44$. While no individual galaxies show detectable H I emission, the emission line signal is detected in the stacked spectra of all subsamples at greater than 4σ significance. The observed total H I 21 cm line flux translates to a H I mass, $M_{\rm H\,I} \approx 10^{10} M_{\odot}$. We find a high H I-to-stellar-mass ratio of $M_{\rm H\,I}/M_{\rm star} \approx 6$ for low-mass galaxies with $\langle \log M_{\rm star}/M_{\odot} \rangle \approx 9.3$ ($>3.7\sigma$). For galaxies with $\langle \log M_{\rm star}/M_{\odot} \rangle \approx 10.6$, we find $M_{\rm H\,I}/M_{\rm star} \approx 0.3$ ($>4.7\sigma$). In addition, the redshift evolution of H I mass, $\langle M_{\rm H\,I} \rangle$, in both low- and high-mass field galaxies, inferred from the stacked emission-line signal, aligns well with the expectation from the cosmic star formation history. This suggests that the overall decline in the cosmic star formation activity across the general galaxy population may be connected to a decreasing supply of neutral hydrogen. Finally, our analysis has revealed significant 21 cm signals at distances greater than 75 kpc from these intermediate-redshift galaxies, indicating a substantial reservoir of H I gas in their extended surroundings.

Unified Astronomy Thesaurus concepts: Catalogs (205); Galaxy evolution (594); H I line emission (690); Radio interferometry (1346)

1. Introduction

Since Cosmic Noon at redshift $z \approx 2$, the cosmic star formation rate density (SFRD) has decreased by nearly a factor of 10 (e.g., P. Madau & M. Dickinson 2014) and possibly larger (e.g., A. M. Matthews et al. 2024). The physical cause of such a dramatic decline remains unclear. Neutral gas is a crucial component in maintaining star formation in galaxies (e.g., F. Walter et al. 2020). The observed decline in cosmic SFRD after $z = 2$ may, therefore, imply a simultaneous change in the properties of neutral gas content of galaxies.

The H I 21 cm line provides a direct method for measuring the neutral gas content of galaxies. However, detecting H I in 21 cm line emission during the "cosmic afternoon" beyond the nearby Universe remains exceedingly challenging with current observational facilities. Direct detections of H I 21 cm emission line from individual galaxies, even at modest redshifts of $z \sim 0.2$–0.3, are either based on selecting

Table 1
Summary of CUBS-MALS Fields

CUBS QSO ID	z_{QSO}[a]	MALS Pointing Center		N_{gal}[b]	Median and 68% Dispersion	
		R.A.	Decl.		z_{gal}	$\log(M_{star}/M_{\odot})$
J0110−1648	0.782	01:10:35.13	−16:48:31.1	743	0.473 [0.314, 0.547]	10.2 [9.3, 10.8]
J0111−0316	1.238	01:12:39.18	−03:28:43.3	361	0.424 [0.315, 0.577]	9.8 [9.0, 10.8]
J0119−2010	0.816	01:19:45.20	−19:58:27.9	532	0.468 [0.350, 0.604]	10.2 [9.2, 10.8]
J0154−0712	1.293	01:54:08.54	−06:52:34.1	551	0.469 [0.369, 0.590]	10.1 [9.2, 10.8]
J0333−4192	1.115	03:31:57.66	−40:58:40.7	478	0.394 [0.320, 0.563]	10.0 [9.1, 10.7]
J0357−4812	1.013	03:57:21.82	−48:12:14.3	419	0.432 [0.332, 0.584]	10.2 [9.2, 10.8]
J0420−5650	0.948	04:20:47.23	−57:12:52.8	609	0.424 [0.269, 0.538]	9.9 [9.0, 10.7]
J2135−5316	0.812	21:34:18.19	−53:35:14.7	665	0.450 [0.330, 0.605]	9.9 [9.1, 10.7]
J2245−4931	1.001	22:45:01.25	−49:31:32.3	578	0.530 [0.354, 0.587]	10.1 [9.2, 10.8]
J2308−5258	1.073	23:07:33.06	−53:12:58.9	487	0.413 [0.325, 0.573]	10.1 [9.2, 10.7]
J2339−5523	1.354	23:39:13.22	−55:23:50.4	563	0.419 [0.294, 0.542]	9.9 [9.0, 10.7]

Notes.
[a] Redshift of the CUBS QSO.
[b] Number of CUBS galaxies in the field.

extremely massive star-forming galaxies (e.g., B. Catinella & L. Cortese 2015) or required several hundred to a few thousand hours of total integration time in small regions of the sky (e.g., A. R. Gogate et al. 2023). As a result, the neutral hydrogen content of individual galaxies beyond $z \approx 0.2$ remains largely unexplored (see M. J. Jarvis et al. 2025).

In contrast, stacking techniques that combine radio maps of galaxies with known redshifts from optical surveys have proven effective in extracting statistically significant H I signals in galaxy populations up to $z \approx 1$ (e.g., A. Chowdhury et al. 2020). At somewhat lower redshifts ($z \approx 0.2$–0.5), stacking measurements based on star-forming galaxies in the COSMOS field (N. Scoville et al. 2007) and the Extended Groth Strip (J. A. Newman et al. 2013) have successfully revealed the mean H I 21 cm emission signal from these galaxies (see results from the uGMRT, MIGHTEE, and MIGHTEE+CHILES surveys; e.g., A. Bera et al. 2023; F. Sinigaglia et al. 2024; A. Bianchetti et al. 2025). However, these measurements exhibit significant scatter, likely due to sample selection effects and variations between different fields caused by cosmic variance (A. Bianchetti et al. 2025, their Figure 7). It is therefore necessary to construct a uniform galaxy sample covering vastly different locations in the cosmos to address possible field-to-field variations.

In this Letter, we report the initial findings of an analysis of stacking H I using deep galaxy survey data from the Cosmic Ultraviolet Baryon Survey (CUBS; H.-W. Chen et al. 2020) and associated radio observations from the MeerKAT Absorption Line Survey (MALS; N. Gupta et al. 2018). Across 11 cosmologically distinct fields, we have assembled a random sample of ≈6000 spectroscopically identified galaxies at $0.24 \leqslant z \leqslant 0.63$ with sensitive H I coverage available from the MALS program. We report new constraints on the H I content of these intermediate-redshift galaxies. The large galaxy sample has also enabled a detailed study of the redshift evolution and stellar mass dependence of H I mass across these 11 fields. Throughout this work, we adopt a flat Λ cosmology with $H_0 = 70\,\mathrm{km\,s^{-1}\,Mpc^{-1}}$ and $\Omega_{M,0} = 0.3$.

2. The Galaxy Sample

To obtain a robust constraint on the H I content of the distant galaxy population, we explore the synergy between the CUBS galaxy sample and the MALS program, one of the early key science programs on the MeerKAT telescope (J. L. Jonas 2018). A summary of galaxy fields with available galaxy survey data and MALS observations is presented in Table 1. Here, we provide a brief summary of the main characteristics of the two programs.

2.1. The CUBS Galaxy Sample

CUBS is a large Hubble Space Telescope (HST) Cycle 25 General Observer Program (PID = 15163; PI: Chen), designed to map diffuse baryonic structures at $z \lesssim 1$ using quasar absorption spectroscopy in 15 UV-bright quasar fields (H.-W. Chen et al. 2020). A critical component of the CUBS program is a comprehensive deep-galaxy survey in these 15 fields, covering an area of angular radius $\theta \lesssim 10'$ from each quasi-stellar object (QSO) sightline. The galaxy spectroscopic survey aims to reach a uniformly high completeness for L_*-type galaxies across each QSO field with progressively deeper depth to uncover fainter galaxies, $\lesssim 0.1\,L_*$, closer to the quasar sightline. This tiered survey design is motivated by the scientific objectives of probing individual gaseous halos on scales of 10–100 kpc using quasar absorption spectroscopy while characterizing the large-scale galaxy clustering environments on scales of 1–5 Mpc.

To optimize the survey efficiency, the wide-field survey prioritizes spectroscopic observations for massive galaxies that are expected to be bright and red with $AB(I) \approx 22.5$ mag and optical colors of $g - r \gtrsim 1.1$ (e.g., S. D. Johnson et al. 2015, see also Figure 1 below). At $z = 0.8$, this survey depth corresponds to $M_B = -20.6$ for a typical spiral galaxy, in comparison to the characteristic absolute magnitude of $M_{B_*} \approx -21$ from random galaxy surveys (see, e.g., S. M. Faber et al. 2007; R. J. Cool et al. 2012). Fainter and bluer galaxies are included as fillers for the slit mask design and are therefore covered at a lower completeness level. Within the inner 3′ region around the QSO, the survey aims to obtain a magnitude-limited sample with $AB(r) > 24$ mag, regardless of the intrinsic color. Redshift measurements are first based on cross-correlation with the Sloan Digital Sky Survey galaxy templates (e.g., H.-W. Chen & J. S. Mulchaey 2009; S. D. Johnson et al. 2013), and then visually inspected by two independent observers. Uncertainties in the redshift

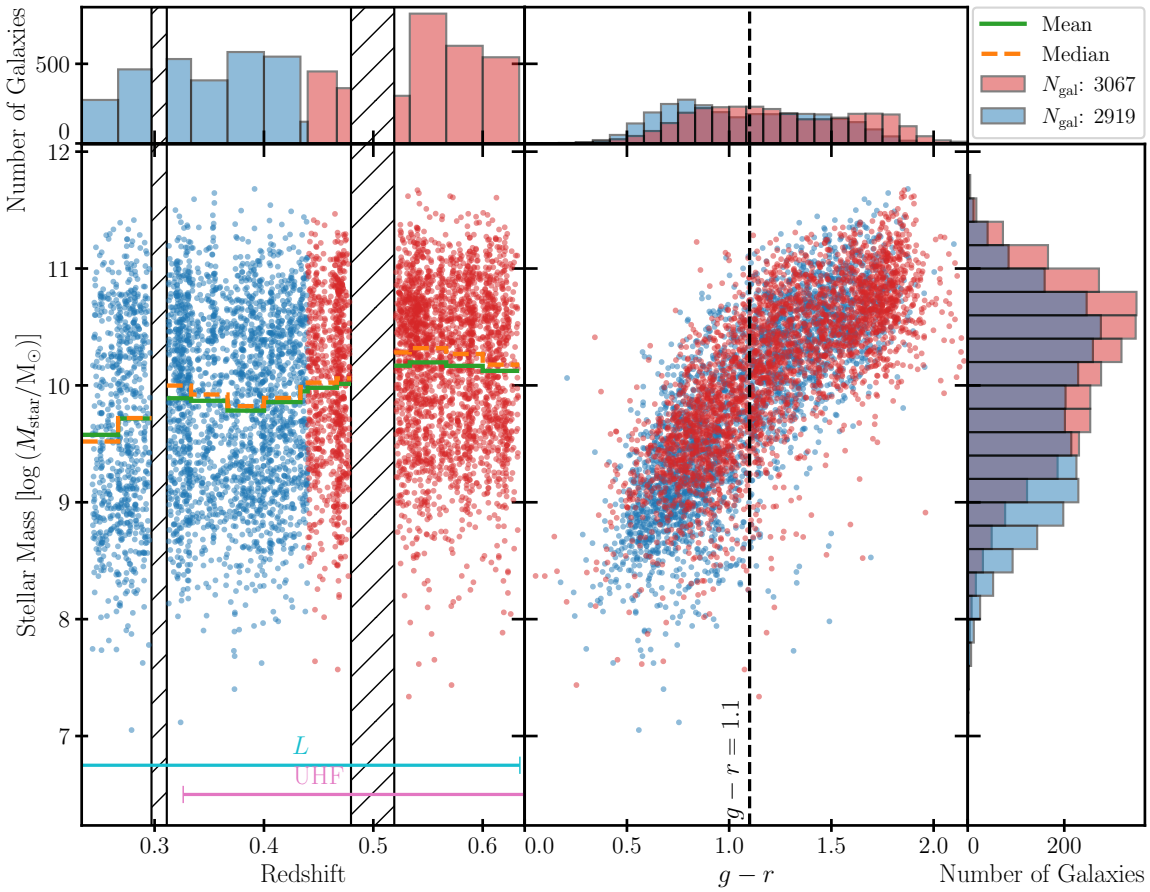

Figure 1. Summary of galaxy properties in the CUBS-MALS galaxy sample. The data points are color coded according to redshift, with galaxies at $z < 0.44$ shown in blue and higher-redshift galaxies in red. The redshift distribution of stellar mass is presented in the left panels. In the bottom panel, the blue and red lines indicate the corresponding redshift coverage of the *L* and UHF bands, respectively. Hatched regions demarcate bands of RFI. Except where truncated by RFI or the samples' boundary, the bins in the histogram of redshifts in the top panel bridge multiples of $\Delta z = 1/30$. The dashed orange and solid green stairs represent the moving weighted median and weighted mean, respectively (see Section 3 for details), within each bin of redshift. The stellar mass vs. the observed $g - r$ color is displayed in the middle panels with the $g - r = 1.1$ color threshold marked by a dashed line. In the histogram of stellar mass in the right panel, the bins span multiples of 0.2 dex. The CUBS-MALS galaxy sample spans a broad range in stellar mass, from $\log M_{star}/M_\odot \approx 8$ to $\log M_{star}/M_\odot \approx 11$, with a median of $\langle \log M_{star}/M_\odot \rangle_{med} \approx 10$ and a wide range in redshift from $z \approx 0.24$ to $z \approx 0.63$ with a median of $\langle z \rangle_{med} = 0.44$. The observed $g - r$ color correlates well with M_{star}, but with a large scatter.

measurements are typically $\Delta v \approx 40\,\mathrm{km\,s^{-1}}$. A complete description and characterization of the galaxy sample will be presented in a future paper (S. D. Johnson et al. 2025, in preparation). In short, for each spectroscopically identified galaxy, we estimate the underlying stellar mass, M_{star}, based on the observed broadband spectral energy distribution using the Bayesian Analysis of Galaxies for Physical Inference and Parameter EStimation code (A. C. Carnall et al. 2018) and a stellar initial mass function (IMF) from P. Kroupa (2002). Uncertainties in M_{star} are typically 0.2 dex, primarily driven by the adopted stellar IMF (D. DePalma et al. 2025, in preparation). A total of 11 of the 15 CUBS QSO fields are also covered by the MALS program. The CUBS-MALS QSO fields are summarized in Table 1.

2.2. MALS Observations

MALS is a large program on the MeerKAT telescope, designed to carry out the most sensitive search of H I 21 cm and OH 18 cm absorption lines at $z < 2$ to establish reliable measurements of the evolution of cold atomic and molecular gas cross sections of galaxies (N. Gupta et al. 2018). The survey covers about 400 pointings centered at radio sources brighter than 200 mJy at 1 GHz in the *L* band, from 900 to 1670 MHz, and the UHF band, from 580 to 1015 MHz. Simultaneously, MeerKAT telescope's large field of view with a full width at half-maximum (FWHM) of $\theta \approx 88'$ at ~1 GHz and excellent sensitivity render it a highly competitive survey for H I 21 cm emission line (e.g., E. Boettcher et al. 2021) and radio-continuum signals (e.g., P. P. Deka et al. 2024; J. D. Wagenveld et al. 2024).

All MALS data are processed using the Automated Radio Telescope Imaging Pipeline (ARTIP; N. Gupta et al. 2021) based on NRAO's Common Astronomy Software Applications (CASA) package (The CASA Team et al. 2022). Detailed descriptions regarding the processing and calibrations of the *L*-band and UHF-band data are presented in N. Gupta et al. (2021) and F. Combes et al. (2021). For spectral-line imaging, the continuous frequency band after calibration is divided into 15 overlapping spectral windows (SPWs) labeled as SPW 0 to SPW 14. Continuum-subtracted visibility data sets for each SPW are processed to produce Stokes-*I* spectral line cubes, which are corrected for the heliocentric motion of the Earth. The corrections for the primary-beam attenuation are applied afterwards.[23]

[23] For the adopted robust = 0 weighting of visibilities, the synthesized beam has a near-Gaussian main-lobe and near-in sidelobes of about 5% (L-band) and 15% (UHF-band) level.

Table 2
Summary of H I Properties for Different CUBS-MALS Subsamples[a]

Sample	z_{gal}	$\log(M_{star}/M_\odot)$	N_{gal}	$\langle z\rangle$	$\langle \log M_{star}/M_\odot\rangle$	$\langle M_{H\,I}\rangle/10^9\ M_\odot$	$M_{H\,I}/M_{star}$
Full	[0.24, 0.63]	[7.1, 11.7]	5986	0.50 ± 0.09	10.0 ± 0.7	13.1 ± 1.3	1.3 ± 0.1
low-z, low-M_{star}	[0.24, 0.44]	[7.1, 10.0]	1319	0.38 ± 0.04	9.2 ± 0.5	8.4 ± 2.2	5.3 ± 1.4
low-z, high-M_{star}	[0.24, 0.44]	[10.0, 11.7]	1600	0.38 ± 0.04	10.5 ± 0.4	10.5 ± 2.1	0.33 ± 0.07
high-z, low-M_{star}	[0.44, 0.63]	[7.1, 10.0]	1827	0.55 ± 0.06	9.4 ± 0.4	16.5 ± 3.1	6.6 ± 1.2
high-z, high-M_{star}	[0.44, 0.63]	[10.0, 11.7]	1240	0.55 ± 0.05	10.6 ± 0.4	13.1 ± 2.5	0.33 ± 0.06

Note.
[a] Errors in $\langle z\rangle$ and $\langle \log M_{star}/M_\odot\rangle$ represent the standard deviation of these quantities within each sample, while errors in $\langle M_{H\,I}\rangle$ represent the 1σ uncertainties based on the rms noise beyond the measurement window of $\pm 250\ km\ s^{-1}$.

For spectral stacks, we focus on galaxies at $0.24 < z < 0.63$ across the 11 CUBS-MALS fields, where the most sensitive constraints for the corresponding 21 cm line are possible with the MALS data. These include 121 spectral-line cubes from SPWs 0–4 in the L band and SPWs 9–14 in UHF. The cubes have a spatial extent of 3 K × 3 K pixels with a pixel size of $2''$ in the L or $3''$ in the UHF band. The typical spatial resolution, as determined by the FWHM of the synthesized beam, is $11''$ at 1100 MHz (corresponding to the observed frequency of the 21 cm line at $z = 0.3$) and $22''$ at 900 MHz (corresponding to the observed frequency of the 21 cm line at $z = 0.6$). The frequency channel spacings for L- and UHF-band cubes are 26.123 and 16.602 kHz, respectively, corresponding to 7.8 and 5.0 km s^{-1} at 1 GHz.

The number of galaxies included in the analysis from each field, as well as median redshift and median M_{star}, are presented in Table 1. Figure 1 presents the redshift distribution of M_{star} (left panel) and M_{star} versus the observed $g - r$ color (middle panel) of the current CUBS-MALS galaxy sample. Note that due to significant radio frequency interference (RFI) in certain frequency ranges, the spectral coverage is effectively not continuous. In summary, the full sample comprises 5986 galaxies with $\log M_{star}/M_\odot \approx 7.1$–11.7 and a median redshift of $\langle z\rangle_{med} \approx 0.44$. The observed $g - r$ color spans a broad range, from $g - r < 0.5$ to $g - r \approx 2$, and correlates strongly with M_{star}. However, the scatter is large, suggesting that additional physical properties may be driving the observed $g - r$ color (e.g., E. F. Bell et al. 2003). To explore how the mean H I content varies with redshift and galaxy properties, we further divide the galaxy sample into four subsamples of low-mass ($\log M_{star}/M_\odot < 10$) and high-mass ($\log M_{star}/M_\odot \geqslant 10$) at $z < 0.44$, and low-mass and high-mass at $z > 0.44$. See Table 2 for details.

3. Stacking Analysis

To measure the mean strength of the 21 cm line signal in intermediate-redshift galaxies, we stack the MALS spectrum at the observed frequency of the redshifted 21 cm line of each galaxy following the steps described here. First, we correct each cube for its primary beam's attenuation using the `katbeam` (version 0.1) model (T. Mauch et al. 2020). Then, for each galaxy, we extract spectral cylinders centered on its systemic redshift with a line-of-sight velocity width of $\pm 1000\ km\ s^{-1}$, and position with a range in diameter from 150 to 600 kpc. Because the size of the synthesized beam is frequency-dependent and the corresponding physical scale per beam also varies with galaxy redshift, we experiment with multiple aperture sizes when extracting the spectra. Specifically, at redshift $z = 0.634$, a FWHM of $22''$ corresponds to roughly 150 kpc in proper distance, representing the coarsest spatial resolution in our MALS dataset. Therefore, we begin with an aperture diameter of 150 kpc—sufficiently large to encompass the expected H I envelope of these galaxies (e.g., A. Bosma 2017; J. Wang et al. 2024)—and increase the aperture size in steps of 150 kpc up to a maximum diameter of 600 kpc. In Section 4.1, we demonstrate that adopting a physical aperture size of 300 kpc delivers the highest quality signals in the stacked spectra.

Next, along the spectral dimension, we subtract residual continuum from each cylinder by fitting a first-order polynomial, excluding the central $\pm 250\ km\ s^{-1}$ window. Note that the radio continuum emission has already been subtracted from the visibilities before making spectral line cubes. Then, we integrate the cylinder over its spatial dimensions to obtain a one-dimensional spectrum in flux density units. To combine individual one-dimensional spectra, we resample each spectrum onto a common velocity grid with a bin size of $\Delta v = 50\ km\ s^{-1}$ and zero velocity corresponding to the systemic redshift of the galaxy. We then coadd individual spectra, $S_i(v)$ of galaxy i, over an ensemble of N galaxies and compute both a weighted mean $\langle S(v)\rangle_{avg}$ and median $\langle S(v)\rangle_{med}$. Because the rms noise in the extracted MALS spectra depends on the primary beam attenuation and the frequency-dependent gain variation of the telescope, the noise between galaxies' spectra varies by a factor of ≈2–3. We therefore apply inverse-variance weighting for each galaxy, where the weight is $w_i = \sigma_i^{-2}/\sum_{i=1}^{N}\sigma_i^{-2}$ with σ_i being the rms noise in the extracted MALS spectrum. For galaxies with both L and UHF coverage, we obtain an average of the L and UHF spectra, applying the same inverse-variance weighting before incorporating these galaxies into the full stack.

We convert the stacked flux spectrum to H I mass spectrum following

$$\left\langle \frac{M_{H\,I}(v)}{M_\odot} \right\rangle = \left(\frac{2.35 \times 10^5}{1+z}\right)\left(\frac{D_L(z)}{\mathrm{Mpc}}\right)^2\left(\frac{\langle S(v)\rangle}{\mathrm{Jy\ km\ s^{-1}}}\right), \quad (1)$$

where D_L is the luminosity distance computed at either the weighted mean or median redshift of each galaxy ensemble (e.g., M. Meyer et al. 2017). The coefficient 2.35×10^5 converts 21 cm photon velocity-integrated fluxes in Jy km s^{-1} to H I mass in units of $M_\odot$. In total, we include 5986 unique galaxies at $0.24 < z < 0.63$, 4783 of which are observed in

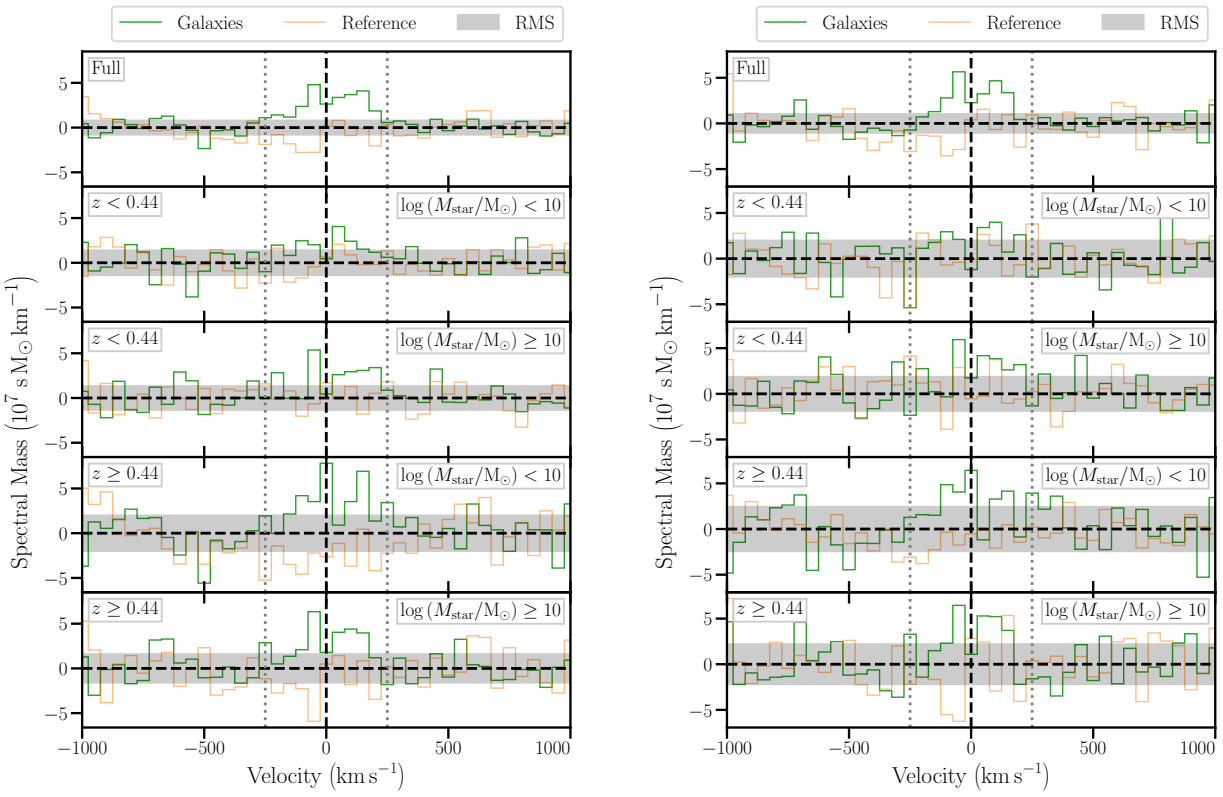

Figure 2. Weighted mean (left) and weighted median (right) spectra of the H I 21 cm emission line extracted using a physical aperture of 300 kpc in diameter around CUBS-MALS galaxies at $0.24 < z < 0.63$. The stacked spectra of CUBS galaxies are shown in thick green, while the reference spectra are shown in thin orange (see Section 3 for details). The gray band marks the rms fluctuations in the error spectrum. The signal associated with the full sample is presented in the top panel, where the signals extracted for individual subsamples are presented in the bottom four rows. The dotted vertical lines mark the velocity window for extracting the total H I mass for each sample. The 21 cm line is confidently detected in all samples with high-z galaxies displaying the strongest signal strength in both low- and high-mass galaxies (bottom two panels). The mean stacks for 150 and 450 kpc diameter apertures are shown in the Appendix.

both L and UHF, leading to 10,887 individual spectra from the L- or UHF-band for stacking.

For each galaxy, we also generate a corresponding reference cylinder at the same redshift but positioned at a randomly chosen location with a sufficiently large offset, ranging from the adopted aperture size to $\approx 4'$, from the science target to prevent blending with the target galaxy. If the randomly selected position overlaps with any known galaxy in the sample, we redraw until a suitable, isolated position is found. These reference cylinders undergo the same processing steps as the science targets, including the extraction of one-dimensional spectra. The resulting spectra are stacked to produce a composite reference spectrum, which serves as a baseline for comparison with the science targets. The results for both the full sample and various subsamples, along with the corresponding reference spectra, are presented in Figure 2.

As shown in Figure 2, the weighted mean and weighted median stacks yield consistent signal strengths, although the weighted median exhibits larger noise fluctuations. Therefore, we focus on the weighted mean spectra in the subsequent analysis. In all subsamples, the stacked 21 cm signals span a broad velocity window from -250 to $+250\,{\rm km\,s^{-1}}$, similar to what has been seen in previous measurements (e.g., A. Chowdhury et al. 2020; H. Guo et al. 2021; A. Bianchetti et al. 2025). As described in Section 2.1, the redshift measurements of CUBS galaxies have uncertainties of only $\Delta v \approx 40\ {\rm km\,s^{-1}}$, well within the spectral bin size. Therefore, the large velocity width of the 21 cm line cannot be attributed to redshift uncertainties. At the same time, galaxies of $\log M_{\rm star}/M_\odot = 11$ typically reside in dark matter halos of mass $\log M_h/M_\odot \approx 13$ (e.g., P. Behroozi et al. 2019) with a corresponding projected line-of-sight virial velocity of $\approx 200\,{\rm km\,s^{-1}}$ at $z = 0.6$. The observed line width suggests a significant contribution from more spatially extended gas in the outskirts of gaseous disks and beyond (see, e.g., J. Wang et al. 2024).

After obtaining the stacked spectrum in mass, we integrate over a velocity window to determine the total H I mass. By experimenting with different velocity widths, we find that a window of $\pm 250\,{\rm km\,s^{-1}}$ captures the full 21 cm line flux while maximizing the significance of the total integrated H I mass.

4. Discussion and Conclusions

By leveraging multisightline galaxy survey data from CUBS and deep radio observations from MALS, we have established a statistically significant galaxy sample from 11 distinct fields to constrain the properties of H I gas at intermediate redshifts (see Figure 1 for a summary of the CUBS-MALS galaxy sample). While no individual galaxies show detectable H I signals, Figure 2 demonstrates that the H I emission line is detected in the stacked spectra of all subsamples at greater than 4σ significance. The observed total 21 cm line flux translates to significant H I mass, which is summarized in Table 2 for individual samples. Uncertainties in $\langle M_{\rm H\,I} \rangle$ are estimated based on the rms noise in the mass spectrum over $500\,{\rm km\,s^{-1}}$ outside of the measurement window. Here, we discuss the

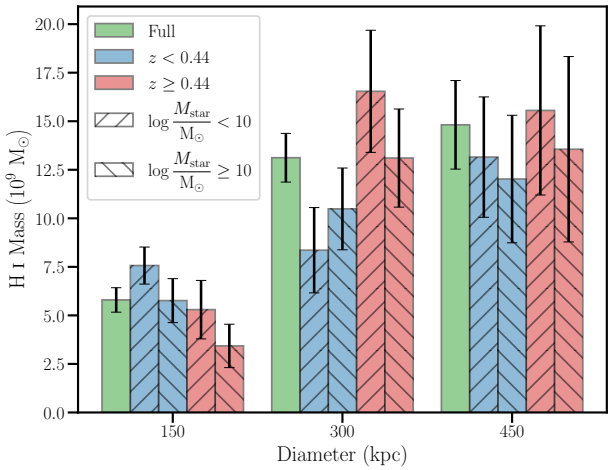

Figure 3. Cumulative mean H I mass with increasing aperture diameter. Doubling the extraction aperture diameter, from 150 to 300 kpc, increases the extracted total H I 21 cm line flux by more than a factor of 2, indicating a significant amount of neutral gas located beyond 75 kpc from the central galaxies, while further increasing the aperture diameter to 450 kpc results in a substantial increase in noise without a corresponding gain in signal (see also Figure A1).

significance and implications for the properties of H I gas in field galaxies at intermediate redshifts.

4.1. Optimal Extraction Apertures and the Spatial Extent of H I

The H I extent of galaxies beyond the local Universe is unknown. Previous studies have adopted an extraction aperture either comparable to the size of the telescope synthesized beam (e.g., A. Bera et al. 2023) or larger (3×; e.g., F. Sinigaglia et al. 2024; A. Bianchetti et al. 2025). This approach is not suitable for the CUBS-MALS sample due to its broad redshift coverage, spanning from $z \approx 0.24$ to $z \approx 0.63$. A fixed angular size would translate into nearly a factor of 2 variation in physical scale between the lowest- and highest-redshift galaxies in our sample, resulting in inconsistent physical volumes probed for H I signals across different epochs (see also M. G. Jones et al. 2016). To address this caveat, we define the extraction aperture size in physical units at the rest frame of each galaxy and select an aperture large enough to enclose the majority of the signal yet sufficiently constrained to preserve the significance of the H I detections around our galaxies.

We examine the stacked H I signal over a range of aperture sizes in multiples of ∼150 kpc in diameter, the largest proper distance corresponding to the beam FWHM—22″ at maximal redshift $z = 0.634$ at 869 MHz among all the fields and the SPWs. We note that an aperture of diameter 150 kpc (75 kpc in radius) is already sufficiently large to cover the largest H I halos known in the local Universe (e.g., J. Wang et al. 2024).

This varying aperture exercise has yielded notable findings. While the 150 kpc diameter aperture produces the highest signal-to-noise ratio in the stacked spectra across all subsamples, the 300 kpc diameter stacked spectrum shows a H I 21 cm line flux more than twice as strong as that measured within the smaller aperture. However, further increasing the aperture size to 450 kpc and beyond provides only marginal gains in the measured H I line flux, as noise begins to dominate (Figure 3; see also Figure A1). We therefore conclude that an aperture diameter of 300 kpc (radius of 150 kpc) is optimal for fully sampling the synthesized beam and for robustly measuring the total H I signal from galaxies across the entire CUBS-MALS redshift range.

The observed increase in the integrated 21 cm line flux when enlarging the aperture from 150 to 300 kpc diameter indicates the presence of significant amounts of H I gas at distances greater than 75 kpc from the CUBS-MALS galaxies. However, because doubling the aperture diameter quadruples the enclosed area, this flux increase corresponds to a factor of ≈3 decline in the mean H I surface mass density, from the inner halo (within 75 kpc) to the outskirts (between 75 and 150 kpc). Such extended reservoirs of H I gas may arise from satellite galaxies and their interactions with central galaxies (e.g., W. J. G. de Blok et al. 2018; H.-W. Chen et al. 2019; J. Wang et al. 2023), or may reflect rapidly cooling and turbulent gaseous halos (e.g., J. Stern et al. 2021).

4.2. Evolution of $M_{H\,I}$ with Redshift

Following the measurements in Table 2, Figure 4(a) shows the weighted mean $M_{\rm H\,I}$ versus redshift for different mass bins. For comparison, we also include the anticipated redshift evolution inferred from the observed cosmic SFRD from P. Madau & M. Dickinson (2014), using the Kennicutt–Schmidt relation to connect star formation with neutral gas (e.g., R. C. Kennicutt 1998).

Specifically, the Kennicutt–Schmidt relation states that the star formation rate (SFR) per unit area ($\Sigma_{\rm SFR}$) is proportional to the neutral gas surface mass density ($\Sigma_{\rm gas}$) according to $\Sigma_{\rm SFR} \propto \Sigma_{\rm gas}^{1.4}$ on galactic scales. The observed cosmic SFRD, $\psi(z)$, is the total SFR summed over all galaxies per unit comoving volume, which can be recast to be the mean SFR averaged over all galaxies multiplied by the comoving number density of galaxies, $\psi(z) = \langle {\rm SFR} \rangle(z) \cdot n_{\rm gal}(z)$. Integrating the Kennicutt–Schmidt relation over the total area of the galaxies leads to ${\rm SFR} \propto M_{\rm gas}^{1.4}$. Given that the number density of galaxies has not evolved strongly within this redshift range (e.g., S. M. Faber et al. 2007), we can further relate the redshift evolution of the cosmic SFRD directly to the anticipated evolution of mean neutral gas mass over the galaxy population between different epochs, following $\langle {\rm SFR} \rangle \propto \langle M_{\rm gas} \rangle^{1.4}$. This is shown as the solid, green curve in Figure 4(a).

Two key features are immediately apparent in Figure 4(a). First, the mean H I content $\langle M_{\rm H\,I} \rangle$ is found to have decreased with increasing cosmic age (or decreasing redshift) by a factor of 2 in low-mass galaxies of $\langle \log M_{\rm star}/M_\odot \rangle \approx 9.3$, from $\langle M_{\rm H\,I} \rangle = (1.7 \pm 0.3) \times 10^{10} M_\odot$ at $\langle z \rangle \approx 0.55$ to $\langle M_{\rm H\,I} \rangle = (8 \pm 2) \times 10^9 M_\odot$ at $\langle z \rangle \approx 0.38$, while a more modest decline is seen in high-mass galaxies of $\langle \log M_{\rm star}/M_\odot \rangle \approx 10.6$, from $\langle M_{\rm H\,I} \rangle = (1.3 \pm 0.3) \times 10^{10} M_\odot$ to $\langle M_{\rm H\,I} \rangle = (1.1 \pm 0.2) \times 10^{10} M_\odot$ over the same period. However, due to large uncertainties, the redshift evolution of $\langle M_{\rm H\,I} \rangle$ for both low- and high-mass galaxies agrees well with that of the cosmic star formation history. Note that a steeper redshift evolution was discussed in A. Bianchetti et al. (2025, their Figure 10) for galaxies of $\log M_{\rm star}/M_\odot \approx 10$, which may be a consequence of inconsistent apertures adopted for different measurements (e.g., H. Guo et al. 2021). Although the uncertainties remain large, the consistent redshift evolution trend between the cosmic SFRD and $\langle M_{\rm H\,I} \rangle$ in galaxies offers tantalizing support for a causal connection between neutral gas and star formation in galaxies.

One notable caveat is the dependence of the observed redshift evolution on the aperture size. The apparent consistency in redshift evolution suggests that a substantial

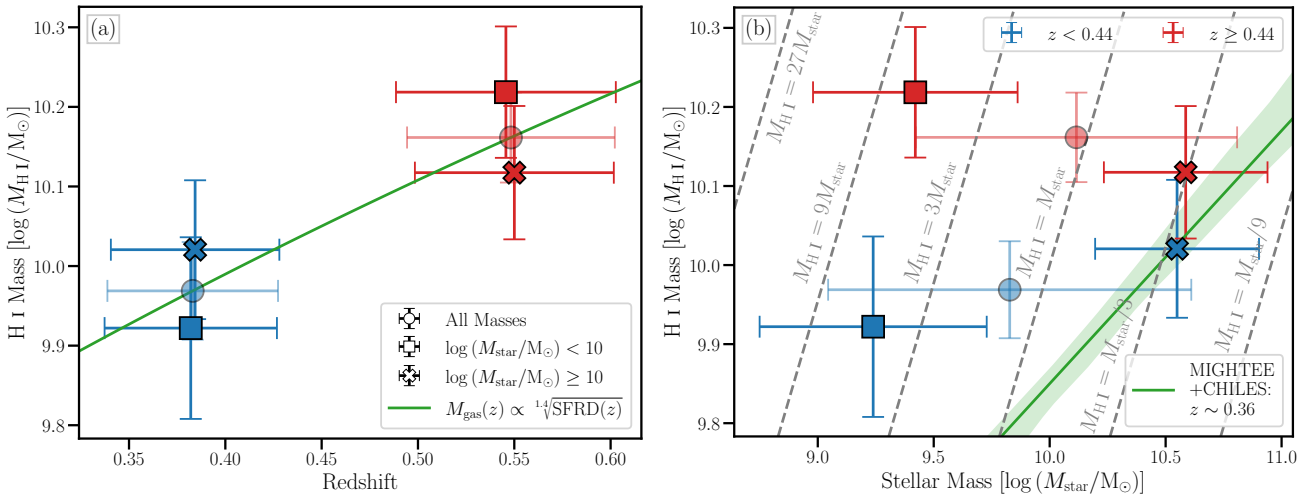

Figure 4. Variation of mean H I mass with redshift (panel (a)) and galaxy stellar mass (panel (b)). Data points and vertical error bars mark the weighted mean H I mass measurements and the associated uncertainties, color coded according to redshift, following what is presented in Figure 1. The horizontal bars indicate the dispersion of each subsample. For comparison, the solid green curve in panel (a) shows the anticipated redshift evolution of neutral gas content inferred from the cosmic star formation rate density (P. Madau & M. Dickinson 2014, Equation (15)), assuming a Kennicutt–Schmidt relation (R. C. Kennicutt 1998, see Section 4.2 for details). The solid green line and the associated shaded band in panel (b) show the scaling relation and uncertainties from the combined MIGHTEE-H I+CHILES study by A. Bianchetti et al. (2025). The gray dashed lines mark fixed $M_{\rm H\,I}/M_{\rm star}$ ratios to facilitate visual calibrations.

fraction of the measured H I mass occurs outside the star-forming interstellar medium (ISM) immediate to the central galaxies (see Section 4.1), whereas the Kennicutt–Schmidt relation is defined for the ISM rather than extended halo gas. One implication is that the accretion timescale for halo H I onto the ISM may be shorter than the star formation (depletion) timescale. To illustrate the impact of aperture choice, we present the observed redshift dependence measured with different extraction apertures in the Appendix.

In addition, the Kennicutt–Schmidt relation is defined for the total neutral gas mass, both atomic and molecular. In our analysis, we use H I as a proxy for the total neutral reservoir, implicitly assuming that the neutral phase is dominated by atomic gas traced by the 21 cm line. However, numerous studies show that the observed SFR correlates more directly with the molecular component (e.g., A. K. Leroy et al. 2008), even though star formation can proceed in predominantly atomic gas in low-metallicity environments such as outer disks and galactic halos (e.g., S. C. O. Glover & P. C. Clark 2012; M. R. Krumholz 2012). While we find consistent redshift evolution between the halo-scale mean H I content and the ISM (disk-scale) SFRD of the general galaxy population, our data lack the spatial resolution to determine whether the 21 cm line-emitting gas is forming stars.

4.3. Variation of $M_{H\,I}$ with Galaxy Mass

An additional goal of our study is to examine how the H I content varies with galaxy mass, which, in our study, is determined by $M_{\rm star}$. Figure 4(b) shows the weighted mean $M_{\rm H\,I}$ versus $M_{\rm star}$ for different redshift bins. For comparison, we also include the best-fit $M_{\rm H\,I}$–$M_{\rm star}$ scaling relation at $z \approx 0.36$ and its associated uncertainties from A. Bianchetti et al. (2025). In addition, the dashed lines mark different constant $M_{\rm H\,I}/M_{\rm star}$ ratios.

We note two new features in Figure 4(b), in addition to the trend of increasing $\langle M_{\rm H\,I}\rangle$ with increasing redshift described in Section 4.2. First, with 1 order of magnitude difference in the mean stellar mass at both low and high redshifts, the H I content remains roughly constant in these galaxies in both epochs. The observed constant $M_{\rm H\,I}$ leads to a factor of ≈18 difference in the $M_{\rm H\,I}/M_{\rm star}$ ratio between low- and high-mass galaxies, with $M_{\rm H\,I}/M_{\rm star} \approx 6$ in galaxies of $\langle \log M_{\rm star}/M_\odot\rangle \approx 9.3$ and $M_{\rm H\,I}/M_{\rm star} \approx 0.3$ in galaxies of $\langle \log M_{\rm star}/M_\odot\rangle \approx 10.6$ at all redshifts probed by our sample. See the last column of Table 2 for the exact values and associated uncertainties.

The observed mass dependence in our sample differs from previous studies, which report a steeper $M_{\rm H\,I}$–$M_{\rm star}$ correlation, specifically $M_{\rm H\,I} \propto {M_{\rm star}}^{0.3}$ (e.g., the results from the joint MIGHTEE-H I+CHILES sample at $z \approx 0.36$; A. Bianchetti et al. 2025). While the $M_{\rm H\,I}/M_{\rm star}$ ratios for the high-mass CUBS-MALS galaxies at both high and low redshifts are consistent with the MIGHTEE-H I+CHILES measurements at lower redshifts, the low-mass CUBS-MALS galaxies show significantly higher $M_{\rm H\,I}/M_{\rm star}$ ratios compared to the MIGHTEE+CHILES results.

4.4. Implications and Potential Systematics

The observed redshift evolution of the mean H I gas mass in galaxies closely tracks the cosmic star formation history, supporting a scenario in which the declining availability of neutral hydrogen drives the overall decrease in the SFR within the general galaxy population. In contrast, previous H I line-intensity mapping and damped Lyα absorber (DLA) studies along random quasar sightlines have reported little to no evolution in the cosmological mean H I mass density at $z \lesssim 1$. Although scatter remains substantial among these measurements (see, e.g., T.-C. Chang et al. 2010; M. Neeleman et al. 2016; F. Walter et al. 2020; and see also H. Guo et al. 2023 for a recent compilation of different measurements) and dust reddening may bias against QSO sightlines intersecting high-N (H I) DLAs—potentially leading to an underestimate of neutral gas mass at high redshifts (e.g., J.-K. Krogager et al. 2019)—the apparent lack of strong evolution in cosmological mean H I mass density has been interpreted as evidence for continuous replenishment of neutral gas reservoirs through accretion or feedback processes (e.g., M. Neeleman et al. 2016).

The discrepancy between the evolution of the H I mass derived from our stacks and that measured by the DLA surveys suggests that these observations may probe neutral gas residing in distinct cosmological volumes. For example, deep multicolor galaxy surveys have shown that the redshift evolution of the SFR per unit mass depends on galaxy mass, with more massive galaxies displaying a more rapid decline in their SFRs over cosmic time compared to lower-mass galaxies (e.g., K. E. Whitaker et al. 2014). Given that the CUBS-MALS galaxy sample is dominated by relatively mature, massive systems located at large angular distances from the QSO sightline (see Section 2.1 and more extensive discussion below), the steep redshift evolution observed in their mean H I gas mass suggests that neutral gas reservoirs associated with mature galaxies diminish more rapidly than those around low-mass star-forming galaxies, which dominate the signals detected by line-intensity mapping and DLA surveys.

At the same time, our findings add further complexity to the already considerable scatter seen among different stacking analyses reported in the literature. In particular, resolving discrepancies in the $M_{\rm H\,I}$–$M_{\rm star}$ scaling relation (Figure 4(b)) is nontrivial, as multiple factors likely influence these results in distinct and nuanced ways.

Fundamental differences between the CUBS-MALS galaxy sample and previous MIGHTEE-H I+CHILES studies include: (1) our galaxy sample is established from 11 distinct fields and therefore less susceptible to potential cosmic variance; (2) relatively mature, massive systems dominate the CUBS-MALS galaxy sample, while previous studies focus primarily on star-forming galaxies; and (3) our analysis employs a large aperture of 300 kpc in diameter for extracting the H I signals, while the MIGHTEE-H I+CHILES measurement is based an aperture of ≈100 kpc (see, e.g., A. Bianchetti et al. 2025).

Given the prioritization of L_* and $g - r > 1.1$ galaxies in the CUBS redshift survey design at $\theta \approx 3'$–$10'$ from the QSO sightlines (see Section 2.1), a substantial fraction of the CUBS-MALS sample likely comprises more mature systems with relatively low H I mass fractions. In light of differences in both sample selection and extraction aperture, the apparent agreement in the mean H I mass between our high-mass subsamples and previous studies in Figure 1(b) is, therefore, somewhat surprising. As shown in Figures 3 and A2, the mean H I mass for the low-z, high-mass subsample measured within a 150 kpc diameter aperture, closer to that adopted by MIGHTEE-H I+CHILES, amounts to only 55% of the value obtained with our fiducial 300 kpc diameter aperture. Taken together, these considerations suggest that, once selection and aperture effects are accounted for, the intrinsic $M_{\rm H\,I}/M_{\rm star}$ ratios of gas-rich, star-forming galaxies are likely higher than implied by existing measurements for high-mass galaxies.

Similarly, the significant difference in the H I content observed for low-mass galaxies may be attributed to aperture loss. As demonstrated in Section 4.1 and in the Appendix, increasing the extraction aperture diameter, from 150 to 300 kpc, leads to a factor of ≈2 increase in the total H I flux. Therefore, the lower $M_{\rm H\,I}$ measurements from the MIGHTEE +CHILES study (based on an extract aperture of triple the FWHM, which is ≈100 kpc in diameter at $z = 0.36$ for CHILES's beam, as the smaller compared to that of MeerKAT) relative to ours may reflect missed 21 cm flux located beyond their extraction aperture.

In summary, we have uncovered significant H I 21 cm signals extending out to a 150 kpc radius around typical galaxies at intermediate redshifts. The H I mass fraction decreases with increasing stellar mass. The redshift evolution of mean H I mass, $\langle M_{\rm H\,I}\rangle$, in both low- and high-mass field galaxies, aligns well with the expectation from the cosmic star formation history. While the inferred $M_{\rm star}$ correlates strongly with the observed $g - r$ color, the large scatter seen in Figure 1 also suggests the presence of a wide range in the star formation histories of individual galaxies (see, e.g., E. F. Bell et al. 2003). A natural next step would be to investigate how the observed H I content depends on the galaxy's star formation history to gain a deeper understanding of the discrepancies reported in the literature. The H I mass measurements based on 21 cm absorption and emission signals from absorption-selected galaxies may also provide clues to the discrepancy concerning constraints from the DLAs.

Acknowledgments

We thank an anonymous referee for the constructive comments that helped improve the presentation of this work. We acknowledge the Massachusetts Institute of Technology's Office of Research Computing and Data for managing the Engaging cluster computer on which this Letter's research was performed. This work is based on observations made with ESO Telescopes at the Paranal Observatory under program ID 0104. A0147(A), observations made with the 6.5 m Magellan Telescopes located at Las Campanas Observatory, spectroscopic data gathered under the HST-GO-15163.01A program using the NASA/ESA Hubble Space Telescope operated by the Space Telescope Science Institute and the Association of Universities for Research in Astronomy, Inc., under NASA contract NAS 5–26555, and imaging spectroscopic data from the MeerKAT telescope. MeerKAT is operated by the South African Radio Astronomy Observatory, which is a facility of the National Research Foundation, an agency of the Department of Science and Innovation. The MeerKAT data were processed using the MALS computing facility at IUCAA (https://mals.iucaa.in/releases). The Common Astronomy Software Applications (CASA) package is developed by an international consortium of scientists based at the National Radio Astronomical Observatory (NRAO), the European Southern Observatory (ESO), the National Astronomical Observatory of Japan (NAOJ), the Academia Sinica Institute of Astronomy and Astrophysics (ASIAA), the CSIRO division for Astronomy and Space Science (CASS), and the Netherlands Institute for Radio Astronomy (ASTRON) under the guidance of NRAO. The National Radio Astronomy Observatory is a facility of the National Science Foundation operated under cooperative agreement by Associated Universities, Inc. N.G. acknowledges the NRAO for its generous financial support for the sabbatical visit to Socorro, during which part of this work was conducted. H.W.C. acknowledges partial support from HST-GO-17517.01A and NASA ADAP 80NSSC23K0479 grants. E.B. acknowledges support from NASA under award number 80GSFC24M0006. S.C. gratefully acknowledges support from the European Research Council (ERC) under the European Union's Horizon 2020 Research and Innovation program grant agreement No. 864361. M.C.C. is supported by the Brinson Foundation through the Brinson Prize Fellowship Program. C.A.F.G. was supported by NSF through grants AST-2108230 and AST-2307327; by NASA

through grants 21-ATP21-0036 and 23-ATP23-0008; and by STScI through grant JWST-AR-03252.001-A. S.L. acknowledges support by FONDECYT grant 1231187.

Facilities: Blanco (DECam), Magellan:Baade (FourStar, IMACS), Magellan:Clay (LDSS-3), MeerKAT, VLT:Yepun (MUSE).

Software: ARTIP (N. Gupta et al. 2021), Astropy (The Astropy Collaboration et al. 2022), CASA (The CASA Team et al. 2022), katbeam (M. S. de Villiers & W. D. Cotton 2022), Matplotlib (J. D. Hunter 2007), NumPy (C. R. Harris et al. 2020), Regions (L. Bradley et al. 2022), SciPy (P. Virtanen et al. 2020), and Spectral-cube (A. Ginsburg et al. 2015).

Appendix
Effects and Implications of Changing Aperture Sizes on the Extracted H I Signals

As discussed in Section 4.1, the nominal aperture size for extracting the H I signal is not known a priori. In principle, robust detection of H I emission depends on matching the aperture size to the spatial extent of the gas. A fundamental limitation in our analysis is set by the telescope's synthesized beam, which corresponds to a diameter of 150 kpc at the maximum redshift $z = 0.634$ in the CUBS-MALS sample. We therefore explore a range of extraction apertures in multiples of 150 kpc. Here we present spectral stacks and the inferred mean H I mass of CUBS galaxies using apertures with diameters of 150 and 450 kpc.

It is clear from comparing the stacked spectra between Figures 2 and A1 that doubling the extraction aperture size, from 150 to 300 kpc, increases the extracted total H I 21 cm line flux by a factor of more than 2. Further increasing the aperture diameter to 450 kpc results in a substantial rise in noise without a corresponding gain in signal. At the same time, Figure A2 shows that the adopted aperture size also has a dramatic impact on the inferred redshift evolution of mean H I mass. In contrast to the increasing mean H I mass with increasing redshift using a 300 kpc diameter aperture, the inferred mean H I mass within a 150 kpc diameter aperture decreases with increasing redshift. However, as described in Section 2.2, the synthesized beam has FWHM $\approx 11''$ corresponding to 50 kpc at $z \approx 0.3$ and FWHM $\approx 22''$ corresponding to 150 kpc at $z \approx 0.6$. A 150 kpc diameter aperture, therefore, corresponds to 3 $\times$ FWHM for low-z galaxies, but merely 1 $\times$ FWHM for the high-z subsample. The apparent trend in Figure A2, therefore, needs to be corrected for differential aperture loss.

We therefore conclude that an extraction aperture of 300 kpc in diameter provides the optimal balance for maximizing the H I signal while minimizing noise and systematic biases. In addition, the substantial increase in the total 21 cm line flux from 150 to 300 kpc diameter aperture has also revealed the presence of substantial H I gas at distances far beyond the stellar body around these galaxies.

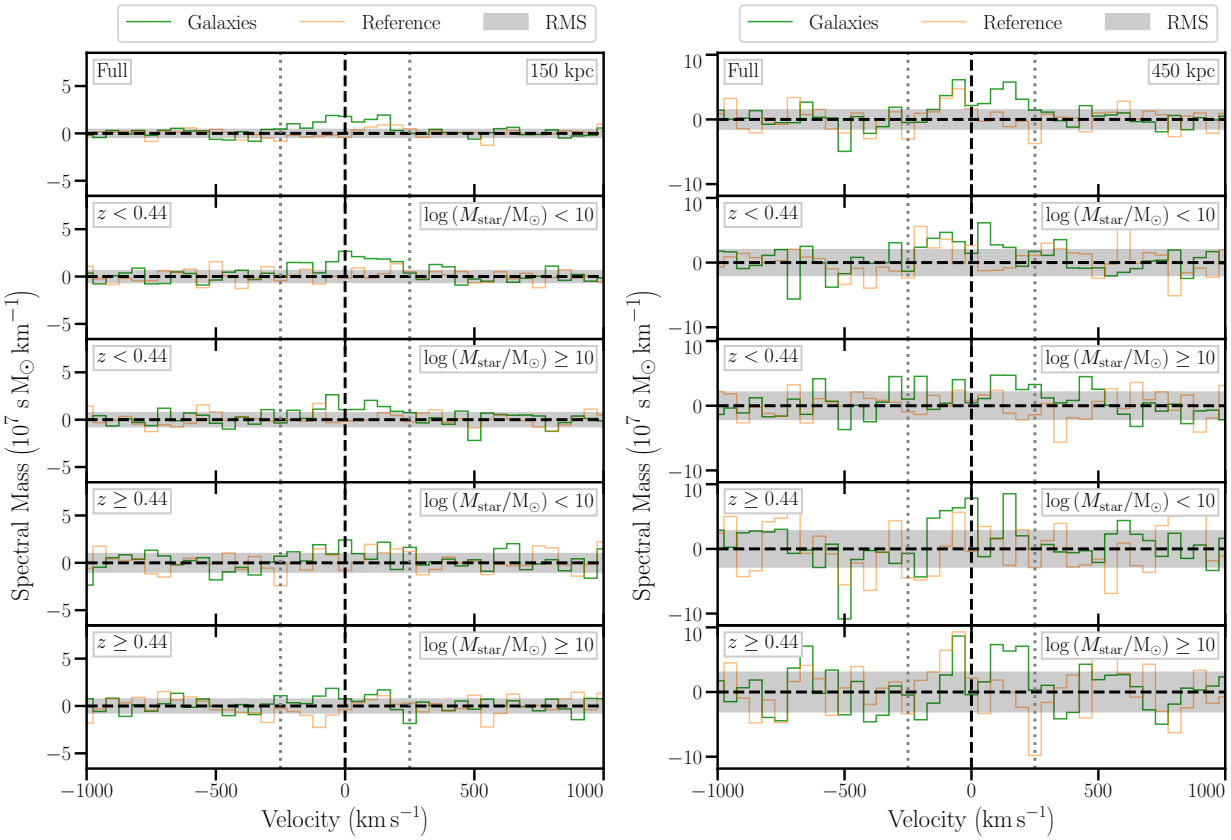

Figure A1. Weighted mean spectral stacks for apertures with diameters of 150 kpc (left) and 450 kpc (right). The remaining details are the same as in Figure 2.

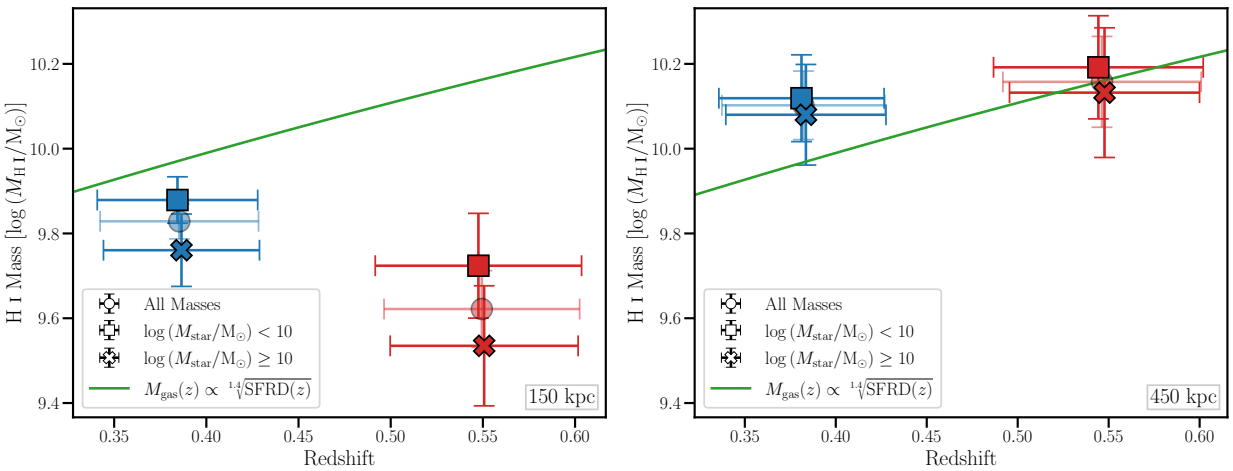

Figure A2. Redshift evolution of measured mean H I mass for apertures with diameters of 150 kpc (left) and 450 kpc (right). The remaining details are the same as in Figure 4.

ORCID iDs

David DePalma https://orcid.org/0009-0003-8927-2140
Neeraj Gupta https://orcid.org/0000-0001-7547-4241
Hsiao-Wen Chen https://orcid.org/0000-0001-8813-4182
Robert A. Simcoe https://orcid.org/0000-0003-3769-9559
Sergei Balashev https://orcid.org/0000-0002-3814-9666
Erin Boettcher https://orcid.org/0000-0003-3244-0409
Sebastiano Cantalupo https://orcid.org/0000-0001-5804-1428
Mandy C. Chen https://orcid.org/0000-0002-8739-3163
Françoise Combes https://orcid.org/0000-0003-2658-7893
Claude-André Faucher-Giguère https://orcid.org/0000-0002-4900-6628
Sean D. Johnson https://orcid.org/0000-0001-9487-8583
Hans-Rainer Klöckner https://orcid.org/0000-0002-0648-2704
Jens-Kristian Krogager https://orcid.org/0000-0002-4912-9388
Jennifer I-Hsiu Li https://orcid.org/0000-0002-0311-2812
Sebastián López https://orcid.org/0000-0003-0389-0902
Pasquier Noterdaeme https://orcid.org/0000-0002-5777-1629
Zhijie Qu https://orcid.org/0000-0002-2941-646X
Gwen C. Rudie https://orcid.org/0000-0002-8459-5413
Joop Schaye https://orcid.org/0000-0002-0668-5560
Fakhri Zahedy https://orcid.org/0000-0001-7869-2551

References

Behroozi, P., Wechsler, R. H., Hearin, A. P., & Conroy, C. 2019, MNRAS, 488, 3143
Bell, E. F., McIntosh, D. H., Katz, N., & Weinberg, M. D. 2003, ApJS, 149, 289
Bera, A., Kanekar, N., Chengalur, J. N., & Bagla, J. S. 2023, ApJL, 950, L18
Bianchetti, A., Sinigaglia, F., Rodighiero, G., et al. 2025, ApJ, 982, 82
Boettcher, E., Chen, H.-W., Zahedy, F. S., et al. 2021, ApJ, 913, 18
Bosma, A. 2017, in in Outskirts of Galaxies, ed. J. H. Knapen, J. C. Lee, & A. Gil de Paz (Cham: Springer), 209
Bradley, L., Deil, C., Ginsburg, A., et al. 2022, astropy/regions v0.10, Zenodo, doi:10.5281/zenodo.5826358
Carnall, A. C., McLure, R. J., Dunlop, J. S., & Davé, R. 2018, MNRAS, 480, 4379
Catinella, B., & Cortese, L. 2015, MNRAS, 446, 3526
Chang, T.-C., Pen, U.-L., Bandura, K., & Peterson, J. B. 2010, Natur, 466, 463
Chen, H.-W., Boettcher, E., Johnson, S. D., et al. 2019, ApJL, 878, L33
Chen, H.-W., & Mulchaey, J. S. 2009, ApJ, 701, 1219
Chen, H.-W., Zahedy, F. S., Boettcher, E., et al. 2020, MNRAS, 497, 498
Chowdhury, A., Kanekar, N., Chengalur, J. N., Sethi, S., & Dwarakanath, K. S. 2020, Natur, 586, 369
Combes, F., Gupta, N., Muller, S., et al. 2021, A&A, 648, A116
Cool, R. J., Eisenstein, D. J., Kochanek, C. S., et al. 2012, ApJ, 748, 10
de Blok, W. J. G., Walter, F., Ferguson, A. M. N., et al. 2018, ApJ, 865, 26
de Villiers, M. S., & Cotton, W. D. 2022, AJ, 163, 135
Deka, P. P., Gupta, N., Jagannathan, P., et al. 2024, ApJS, 270, 33
Faber, S. M., Willmer, C. N. A., Wolf, C., et al. 2007, ApJ, 665, 265
Ginsburg, A., Robitaille, T., Beaumont, C., et al. 2015, in in Revolution in Astronomy with ALMA: The Third Year, ed. D. Iono et al. (San Francisco: ASP), 363
Glover, S. C. O., & Clark, P. C. 2012, MNRAS, 421, 9
Gogate, A. R., Verheijen, M. A. W., van der Hulst, J. M., & Jaffé, Y. L. 2023, MNRAS, 519, 4279
Guo, H., Jones, M. G., Wang, J., & Lin, L. 2021, ApJ, 918, 53
Guo, H., Wang, J., Jones, M. G., & Behroozi, P. 2023, ApJ, 955, 57
Gupta, N., Jagannathan, P., Srianand, R., et al. 2021, ApJ, 907, 11
Gupta, N., Srianand, R., Baan, W., et al. 2018, in Proc. of MeerKAT Science: On the Pathway to the SKA, 277, ed. R. Taylor (Trieste: SISSA), 14
Harris, C. R., Millman, K. J., van der Walt, S. J., et al. 2020, Natur, 585, 357
Hunter, J. D. 2007, CSE, 9, 90
Jarvis, M. J., Tudorache, M. N., Heywood, I., et al. 2025, MNRAS, Advance Access
Johnson, S. D., Chen, H.-W., & Mulchaey, J. S. 2013, MNRAS, 434, 1765
Johnson, S. D., Chen, H.-W., & Mulchaey, J. S. 2015, MNRAS, 449, 3263
Jonas, J. L. 2018, in MeerKAT Science: On the Pathway to the SKA, 277, ed. R. Taylor (Trieste: SISSA), 1
Jones, M. G., Haynes, M. P., Giovanelli, R., & Papastergis, E. 2016, MNRAS, 455, 1574
Kennicutt, R. C., Jr. 1998, ApJ, 498, 541
Krogager, J.-K., Fynbo, J. P. U., Møller, P., et al. 2019, MNRAS, 486, 4377
Kroupa, P. 2002, Sci, 295, 82
Krumholz, M. R. 2012, ApJ, 759, 9
Leroy, A. K., Walter, F., Brinks, E., et al. 2008, AJ, 136, 2782
Madau, P., & Dickinson, M. 2014, ARA&A, 52, 415
Matthews, A. M., Kelson, D. D., & Newman, A. B. 2024, ApJ, 966, 194
Mauch, T., Cotton, W. D., Condon, J. J., et al. 2020, ApJ, 888, 61
Meyer, M., Robotham, A., Obreschkow, D., et al. 2017, PASA, 34, 52
Neeleman, M., Prochaska, J. X., Ribaudo, J., et al. 2016, ApJ, 818, 113
Newman, J. A., Cooper, M. C., Davis, M., et al. 2013, ApJS, 208, 5
Scoville, N., Aussel, H., Brusa, M., et al. 2007, ApJS, 172, 1
Sinigaglia, F., Rodighiero, G., Elson, E., et al. 2024, MNRAS, 529, 4192
Stern, J., Sternberg, A., Faucher-Giguère, C.-A., et al. 2021, MNRAS, 507, 2869
The Astropy Collaboration, Price-Whelan, A. M., Lim, P. L., et al. 2022, ApJ, 935, 167
The CASA Team, Bean, B., Bhatnagar, S., et al. 2022, PASP, 134, 114501
Virtanen, P., Gommers, R., Oliphant, T. E., et al. 2020, NatMe, 17, 261
Wagenveld, J. D., Klöckner, H. R., Gupta, N., et al. 2024, A&A, 690, A163
Walter, F., Carilli, C., Neeleman, M., et al. 2020, ApJ, 902, 111
Wang, J., Lin, X., Yang, D., et al. 2024, ApJ, 968, 48
Wang, J., Yang, D., Oh, S. H., et al. 2023, ApJ, 944, 102
Whitaker, K. E., Franx, M., Leja, J., et al. 2014, ApJ, 795, 104